# Direct probe of Fermi surface evolution across a pressure-induced quantum phase transition

Yejun Feng,[1,2] A. Palmer,[2] Yishu Wang,[2] D. M. Silevitch,[2] and T. F. Rosenbaum[2,3]
[1]*The Advanced Photon Source, Argonne National Laboratory, Argonne, Illinois 60439, USA*
[2]*The James Franck Institute and Department of Physics, The University of Chicago, Chicago, Illinois 60637, USA*
[3]*Division of Physics, Mathematics, and Astronomy, California Institute of Technology, Pasadena, California 91125, USA*
(Received 27 October 2014; revised manuscript received 6 April 2015; published 24 April 2015)

The nature of a material's Fermi surface is crucial to understanding its electronic, magnetic, optical, and thermal characteristics. Traditional measurements such as angle-resolved photoemission spectroscopy and de Haas–van Alphen quantum oscillations can be difficult to perform in the vicinity of a pressure-driven quantum phase transition, although the evolution of the Fermi surface may be tied to the emergence of exotic phenomena. We demonstrate here that magnetic x-ray diffraction in combination with Hall effect measurements in a diamond anvil cell can provide valuable insight into the Fermi surface evolution in spin- and charge-density-wave systems near quantum phase transitions. In particular, we track the gradual evolution of the Fermi surface in elemental chromium and delineate the critical pressure and absence of Fermi surface reconstruction at the spin-flip transition.

DOI: 10.1103/PhysRevB.91.155142 PACS number(s): 75.30.Fv, 64.70.Tg, 71.18.+y, 74.62.Fj

## I. INTRODUCTION

The need to delineate the electronic and magnetic character of a material becomes particularly acute at a phase transition. The evolution of a metal's Fermi surface often provides the key. When the transition occurs at zero absolute temperature, the complexity grows. As with many aspects of quantum phase transitions, such as the influence of quantum fluctuations and changes in scaling exponents and universality classes [1], the evolution of the Fermi surface is not always understood and often difficult to measure. In metal-insulator transitions, a potential violation of Luttinger's theorem demands either a first-order transition or non-Fermi-liquid behavior [2]. In antiferromagnetic heavy fermions, the change of Fermi surface is possibly related to the localization of itinerant charge carriers [3], and non-Fermi-liquid behavior has become a common theme [4]. Experimentally, however, parsing Fermi surface changes is difficult, especially when the quantum phase transition is driven by pressure. Angle-resolved photoemission spectroscopy (ARPES) requires samples in vacuum with well-prepared surfaces [5,6], while de Haas–van Alphen (dHvA) and Shubnikov–de Haas quantum oscillation techniques require large magnetic fields, which can result in structural or electronic changes to the system.

$2k_F$-density wave systems have been discussed extensively as a class of materials for studying continuous quantum phase transitions and related quantum critical behavior [7–10]. These systems encompass many types of Fermi surface instability, such as nesting [11], saddle points [12], and hot spots [7–10], and could even extend to quasiparticle interference in high-$T_c$ cuprates, where the ordering wave vector at a given energy is strongly dependent on the detailed dispersion of the band structure near the Fermi surface [13]. In general, incommensurate charge and spin order [14] can arise from local entities, through mechanisms such as electron-phonon coupling [15–17] and Ruderman-Kittel-Kasuya-Yosida (RKKY) exchange interactions [18]. On the other hand, itinerant instabilities have been identified in many incommensurate charge-density wave (CDW) and spin-density wave (SDW) materials [11,19–21], and those $2k_F$ systems are often sensitive to athermal tuning parameters such as chemical doping and alloying [6,19,20], impurities [22], and pressure [23,24]. The Fermi surfaces of these $2k_F$ systems at ambient pressure are often calculable with *ab initio* band-structure calculations [6,25,26] and are directly measureable through techniques such as ARPES [5,6]. The pressure evolution of the incommensurate ordering wave vectors can be measured directly using diffraction techniques [24,27,28] to reflect features on the Fermi surface [7–10,19–21].

While diffraction of the $2k_F$ wave vector probes the gapped part of the Fermi surface, an independent measurement of the remaining itinerant carriers is necessary to fully explore the Fermi surface evolution. Compatibility with pressure, a common tuning parameter for such systems, is highly desirable. Hall effect measurements offer suitable sensitivity to changes in the Fermi surface consonant with a pressure-cell environment.

Here, we use a combination of x-ray diffraction and Hall measurements to provide insight into the evolution of the Fermi surface in the spin-density-wave antiferromagnet chromium over a large range in pressure-temperature phase space, including a pressure-driven, spin-flip quantum phase transition. Spin-flip transitions are common phenomena in many types of antiferromagnets [21,29–31] and often can be tuned by external parameters such as magnetic field [29,32], pressure [33], and even surface boundary conditions [30]. In $2k_F$ spin-density wave antiferromagnets, the spin orientations are not necessarily constrained by the Fermi surface instability [30]. Nevertheless, in certain cases the first-order spin-flip transition is sufficiently strong to drive a discontinuous change in the wave vector $\boldsymbol{Q}$ [21].

## II. EXPERIMENTAL METHODS

Nonresonant magnetic diffraction under pressure was carried out at beamline 4-ID-D of the Advanced Photon Source using horizontally polarized 20-keV x rays diffracting in the vertical plane [27,28,34]. A major improvement over previous work [34] was to utilize a pair of wide-angle ($60^\circ$ $2\theta$) perforated diamond anvils [28] (Fig. 1) to significantly reduce the elastic background.

 

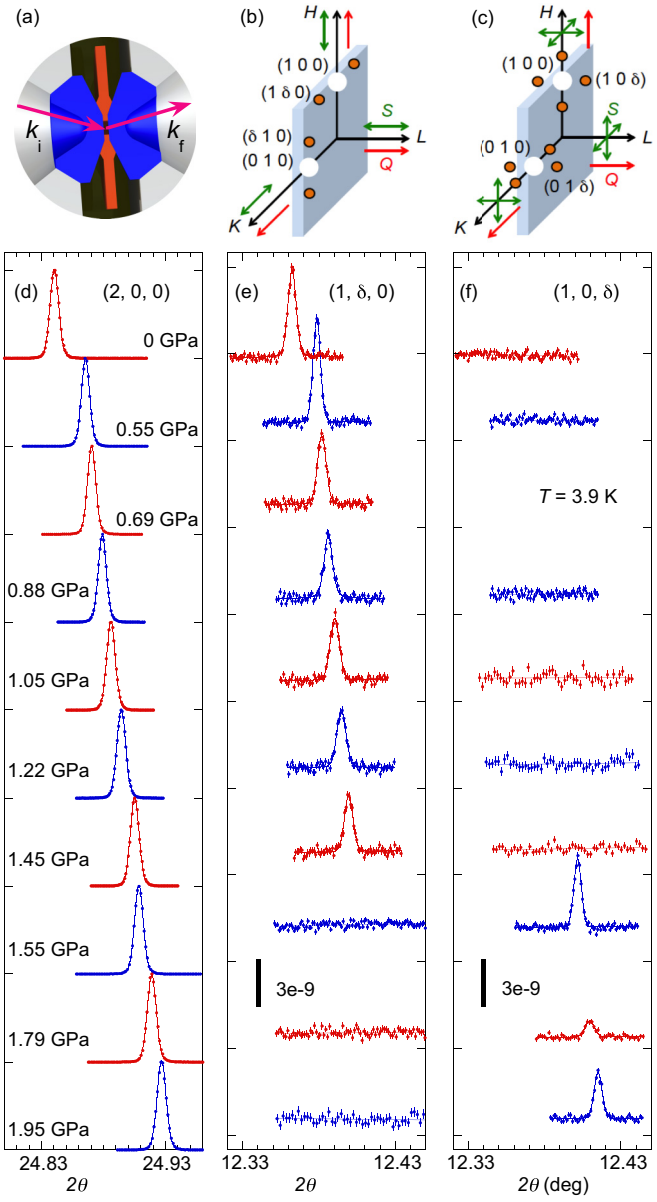


FIG. 1. (Color online) (a) Physical geometry of x-ray diffraction within the high-pressure diamond anvil cell. A pair of wide-angle-perforated diamond anvils (blue) [28] and a gasket (orange) confine the pressure chamber containing the sample (not shown). Arrows show incident and scattered x-ray beam paths. (b, c) Spin structures and magnetic diffraction patterns for the longitudinal and transverse SDW in Cr, respectively. While diffraction of the (1,0,0) lattice order (white circles) is forbidden, different diffraction patterns of the SDW (orange circles) are present depending on whether spins $\boldsymbol{S}$ (green arrows) are longitudinal or transverse to the ordering wave vector $\boldsymbol{Q}$ (red arrows). Representative longitudinal ($\theta/2\theta$) scans of (d) lattice order (2, 0, 0), and SDW orders of (e) (1, $\delta$, 0) and (f) (1, 0, $\delta$) at ten different pressures. All lattice peaks are normalized to unity, while vertical bars in (e) and (f) represent the scale of relative intensity for SDWs to their respective (2,0,0) order. All peaks are fit with a pseudo-Voigt form and a linear background. The spin-flip transition is between 1.45 and 1.55 GPa. The variation of magnetic diffraction intensity in (e) and (f) is due to the change of degenerate SDW domains along a particular cubic axis under pressure [27].

The cubic lattice in the paramagnetic phase of Cr allows a threefold degeneracy of $\boldsymbol{Q}$ along each of the cubic axes. For each $\boldsymbol{Q}$, the SDW is either longitudinal to $\boldsymbol{Q}$ or along two transverse directions. In addition, there is a CDW as a second harmonic of the SDW with a wave vector $2\boldsymbol{Q}$ [35]. Single-crystal Cr samples (99.996%, Alfa Aesar) were prepared as square plates with typical size $80 \times 80 \times 40\,\mu\text{m}^3$ [36] for scattering-optimized diamond anvil cells. The samples were aligned with the surface normal of the plate oriented along the [0,0,1] direction, which is approximately parallel to the compression axis of the pressure cell upon loading. The sample, high-pressure cell, and diffraction geometry allowed x-ray magnetic diffraction to be performed with the azimuthal vector (0,0,1) inside the diffraction plane, and accessing the $(1, \pm\delta, 0)/(\pm\delta, 1, 0)$, $(0, 1, \pm\delta)/(1, 0, \pm\delta)$ orders.

The cross section of nonresonant x-ray magnetic diffraction is in practice only sensitive to the out-of-plane spin component $S_\perp$ [37]. For the azimuthal vector (0,0,1) inside the diffraction plane, only the $(1, \pm\delta, 0)$ and $(\pm\delta, 1, 0)$ orders are observable in the longitudinal spin structure. For the same azimuthal condition in the transverse spin configuration, the $(1, 0, \pm\delta)$ and $(0, 1, \pm\delta)$ orders become observable (Fig. 1), while diffraction of $(1, \pm\delta, 0)$ and $(\pm\delta, 1, 0)$ is no longer present. Thus, measuring these sets of diffraction orders can determine whether the sample has longitudinal or transverse spin order or coexisting domains of both structures.

Both CDWs and SDWs were probed in detail at five different pressures. The SDW intensity $I_{\text{SDW}}$ was measured for SDWs around (1,0,0) or (0,1,0), with a summation of $(0,1,\delta)$ and $(1,0,\delta)$ to account for the degenerate transverse-SDW (TSDW) along the $L$ domain. The CDW intensity $I_{\text{CDW}}$ was measured around the (2,0,0), (1,1,0), and (2,1,1) orders before converting to that of the $(2Q,0,0)$ order. The wave vector $Q$ was determined at each pressure by averaging over measurements of five to fourteen different CDW/SDW orders, with CDWs around the (2,0,0), (1,1,0), and (2,1,1) orders and SDWs around (1,0,0). The widths of both the lattice and magnetic diffraction peaks are all instrument resolution limited in Fig. 1; thus the pressure inhomogeneity over the Cr sample is estimated to be less than 0.04 GPa at the spin-flip transition [34]. The observation of CDWs along all three cubic axes also rules out significant pressure anisotropy [34].

For the transport measurements, polycrystalline Cr samples (99.999% pure, ESPI Metals) of $150 \times 150 \times 30\,\mu\text{m}^3$ size were prepared in a manner similar to the single-crystal diffraction samples [36], except the raw material was first thermally annealed at 1050 °C for 20 h in an $\text{Ar}/\text{H}_2$ (85%/15%) mixture atmosphere. Since $R_{\text{H}}$ of Cr is largely isotropic [38], we chose to use polycrystalline specimens because of the available higher level of purity. Four gold leads were spot-welded in the van der Pauw geometry to every Cr sample [39]. Data presented here were measured on three polycrystalline Cr samples, with an ambient-pressure residual resistivity ratio of 70–110 between 300 and 4 K, and a 4-K resistivity at all pressures with $\rho_0 = 0.10 - 0.14\,\mu\Omega\,\text{cm}$. Electrical measurements were carried out in a Physical Property Measurement System (Quantum Design, Inc.) using a pressure cell designed for measurements in the multidimensional $H$-$P$-$T$ space [40]. Sapphire seats and thermally hardened MP35N gaskets were

used to minimize magnetic field distortion. The resistivity in the Hall geometry $\rho_{xy}(H)$ was measured between $\pm 0.5$ T using a Lakeshore 370 ac resistance bridge and a Lakeshore 3708 preamplifier. Given the typical residual resistivity $\rho_0$, the field range puts our Hall measurement in the low field limit with $\omega_c \tau < 1$ [41], where $\omega_c$ is the cyclotron frequency. The antisymmetrized $\rho_{xy}(H)$ component was fit to a polynomial form, and the linear component in field was used to calculate $R_H$. This procedure eliminates other spurious contributions to $\rho_{xy}(H)$ such as conventional longitudinal magnetoresistance.

## III. RESULTS

For Cr at ambient pressure, the electronic and spin structures are both well understood [5,25,26,35,42]. The electronic structure of paramagnetic Cr has four bands at the Fermi surface: an electron octahedron at reciprocal lattice point Γ, a hole octahedron at H with a matching (nested) shape, and two types of ellipsoids that act as charge reservoirs [25]. One type of ellipsoid is electronlike and resides between the two nesting bands along the ⟨1, 0, 0⟩ or Γ−H direction. The other is holelike and is isolated along the ⟨1, 1, 0⟩ direction at reciprocal point N. Upon the formation of the spin density wave, itinerant spins are aligned transverse to the wave vector $\boldsymbol{Q} = (1-\delta, 0, 0) \sim (0.952, 0, 0)$ between $T_N = 311$ K and the spin-flip transition temperature $T_{SF} = 123$ K, and parallel (longitudinal) to $\boldsymbol{Q}$ below $T_{SF}$ (Fig. 1). For Cr at ambient pressure, there is no sign of an abrupt change in itinerant carriers at $T_{SF}$, judging from both the electrical resistivity [23,35] and Hall coefficients [38].

It is known that hydrostatic pressure quickly suppresses the formation of the longitudinal spin configuration in Cr [33]. However, the detailed $P$-$T$ space phase boundary has not been elucidated. The changes in spin configuration only can be probed directly by neutron and x-ray diffraction. Neutron magnetic diffraction demonstrated a monotonic reduction of $T_{SF}(P)$ to 90 K at $P = 0.6$ GPa [33], and previous x-ray magnetic diffraction offered only a coarse boundary at $P \sim 1$ GPa for $T < 8$ K [27]. Here we first finely delineate the spin-flip transition in Cr using the nonresonant x-ray magnetic diffraction technique (Fig. 1). The spin-flip transition is clearly manifested in Fig. 1 by the switch in observed SDW diffraction signals from $(1, \pm\delta, 0)$ and $(\pm\delta, 1, 0)$ to $(1, 0, \pm\delta)$, whereas the CDWs along all three cubic axes were observed at 1.45, 1.55, and 1.95 GPa (Fig. 2). Within the resolution of our pressure tuning capability, no phase coexistence was observed, and the boundary of the spin-flip transition can be precisely determined to be $1.50 \pm 0.05$ GPa at $T = 3.9$ K.

Given that the wave vector $Q$ is reflective of the nesting condition at the Fermi surface [35], x-ray diffraction provides direct insight into the evolution of the nesting bands under pressure. The overall change in $Q$ with increasing $P$ indicates a change of both electron and hole octahedron sizes in the paramagnetic phase. This is likely due to a charge-transfer effect under pressure. However, no discontinuity in $Q$ larger than 0.0004 r.l.u. was observed at the spin-flip transition [Fig. 2(c)], which rules out strong modifications of the two nesting bands at the pressure-driven quantum phase transition.

The overall evolution of the Fermi surface is probed by Hall effect measurements from 0 to 7.6 GPa in pressure and

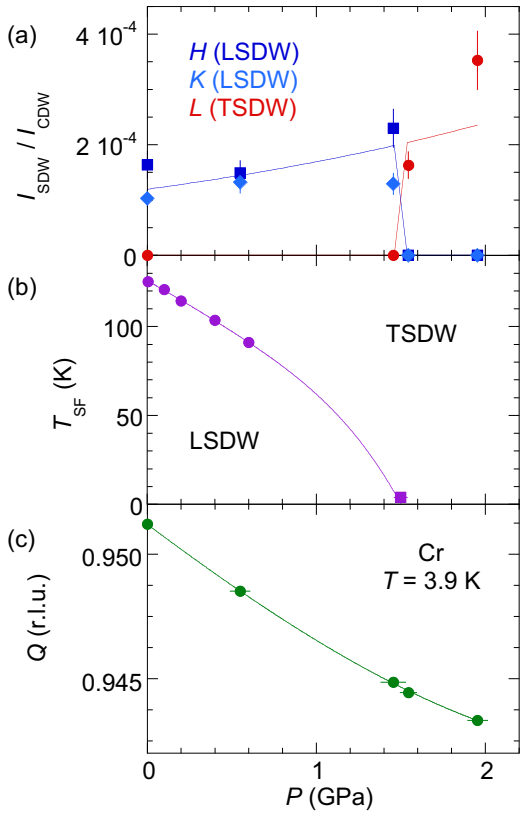


FIG. 2. (Color online) (a) Following the geometrical notation of Figs. 1(b) and 1(c), the relative intensities $I_{SDW}/I_{CDW}$ are separately tracked for individual cubic domains as a function of pressure. All show consistent behavior with the spin-flip phase transition. In this low-pressure range, both $I_{SDW}$ and $I_{CDW}$ decrease exponentially as a function of pressure [27]. Due to the scaling relationship $I_{SDW} \sim I^2_{CDW}$, all nonzero ratios of $I_{SDW}/I_{CDW}$ increase with an exponential functional form. (b) Magnetic $P$-$T$ phase diagram of Cr. The phase line between transverse (TSDW) and longitudinal (LSDW) phases is determined by neutron magnetic diffraction (circles) [33] and current x-ray magnetic diffraction (square) under pressure. (c) SDW wave vector $Q$ as a function of pressure. Solid lines are guides to the eye.

2–350 K in temperature (Fig. 3). The pressure range of this measurement extends to well above the measured 1.5 GPa spin-flip transition pressure. The $\pm 0.5$ T applied field used in these Hall measurements is much smaller than the field required to perform dHvA measurements in chromium [35,43] and causes no observable field-induced magnetostriction effect [44]. Our measured $R_H$ at $P = 0$ (Fig. 3) is consistent with results in the literature [38], with a sharp rise in $R_H$ marking the opening of the SDW gap at $T_N = 311$ K and the gradual saturation with decreasing temperature at approximately $T_N/2$. Below 140 K, $R_H$ is nonmonotonic in temperature, with a sharp dip anomaly occurring at $T \sim 35$ K. The pressure evolution of $R_H(T)$ exhibits several major trends. The high-temperature rise in $R_H$ at $T_N(P)$ moves to lower temperature with increasing pressure, consistent with the pressure dependence of $T_N(P)$ in Cr [23]. By contrast, the 35 K dip feature in $R_H$ remains stable under increasing pressure, although its depth gradually reduces.

Similar dip features in $R_H$ were observed in high-quality metals such as Cu, Ag [41], and single-crystalline Mo [45] and W [46]. There exist several theories for the feature

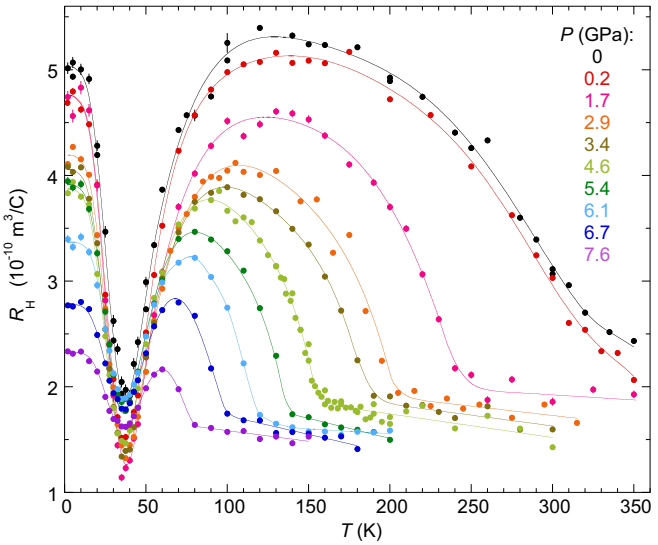


FIG. 3. (Color online) Hall coefficient $R_H(T,P)$. The evolution of the Néel transition with $P$ is marked for pressures from 0 to 7.6 GPa. The low-temperature dip at $T \sim 35$ K remains essentially unchanged over the large pressure range, including the spin-flip transition, mitigating against any Fermi surface reconstruction.

[38,41,46,47]. The simplest explanation of the dip anomaly involves a competition of two relaxation times $\tau$ of itinerant electrons, originating from either Fermi surfaces of different topology and curvature such as belly and neck [41], or phonon scattering channels of normal vs Umklapp processes [38,46,47]. While increases in impurity and disorder scattering have been experimentally shown to suppress the dip feature in $R_H$, these effects simultaneously reduce the characteristic temperature and depth [41]. By contrast, we see in Fig. 3 that the dip feature remains constant in temperature at 35 K for the entire pressure range, indicating that the pressurization process has not substantially increased the role of disorder; similarly, we see a flat residual resistivity $\rho_0(P)$ [39]. This suggests that the processes driving the diminution of the dip depth alone are intrinsic to the itinerant electrons on the Fermi surface.

For Mo and W, the Fermi surfaces are similar in shape and size to that of paramagnetic Cr, but without an itinerant instability capable of inducing a SDW state [25,26,35]. Thus a comparison of all three systems helps to illustrate microscopic details of the dip feature in $R_H$. It has been suggested that the dip anomaly in $R_H$ is due to the Umklapp process between the non-nesting electron ellipsoid along the Γ-H direction and the tip of the large hole octahedron at H [46]. The hole octahedron seems to retain part of its density of states after the formation of an SDW [5], since it is larger than the electron octahedron in Cr. This Umklapp process is highly dependent on the anisotropy of the electron relaxation time $\tau(\boldsymbol{k})$ [38,46,47], which is in turn sensitive to the small separation between the two bands in reciprocal space. Hence the dip feature in $R_H$ appears to sensitively trace the small distance variation between hot spots on the Fermi surface. The reduction of $R_H$ dip depth under pressure signals a decreasing importance of Umklapp scattering with a growing isotropic electron relaxation time. This in turn indicates that the close proximity between the electron ellipsoid and the large nesting hole octahedron slowly increases over our measured pressure range.

## IV. DISCUSSION

Our x-ray magnetic diffraction and electrical Hall coefficient results reveal the pressure evolution of several reciprocal space distances between the two nested bands and from one charge ellipsoid to the hole octahedron, respectively. The charge-transfer process in those three bands is gradual across a wide $P$-$T$ phase space, without abrupt change at the spin-flip quantum phase transition. In addition, our measured $R_H(T = 2\,\mathrm{K}, P)$ drops slowly and continuously with increasing pressure, correlating well with the reduction of the SDW gap size under pressure. A quantitative calculation of $R_H$ for a four-band model in Cr is difficult due to the differing carrier mobilities in the various bands [38]. However, being charge reservoirs, the hole and electron ellipsoids possess the majority of the remaining itinerant carriers in the low-temperature limit of the gapped state of the SDW. In the case of an abrupt Fermi surface reconstruction, the sudden change in the hole/electron ratio would noticeably alter $R_H$. This suggests that there are no dramatic changes in any of the four bands at the pressure-induced spin-flip transition, which is consistent with a continuously evolving lattice (Fig. 1) and no detectable change of symmetry [48] seen by x-ray diffraction. Our results show that for itinerant spin systems a spin-flip quantum phase transition does not necessarily involve noticeable Fermi surface reconstruction, despite the clear first-order nature of the transition.

Fermi surface evolution at quantum phase transitions traditionally has been characterized by dHvA techniques [49,50]. This is true as well for Cr under pressure. Thus it is instructive to compare results from that approach to ours. Quantum oscillation measurements [43] reported a spin-flip transition at $P = 0.93 \pm 0.01$ GPa and $T = 2$ K, and a simultaneous significant reconstruction of the Fermi surface. Our current work disagrees with these measurements in both the value of the critical pressure and the claim of a massive Fermi surface reconstruction associated with the spin-flip transition.

We note that the dHvA work was carried out in a magnetic field ranging from 8 to 34 T [43]. The $H$-$T$ phase diagram of the SDW in Cr is not well understood at ambient pressure [32,35]. While the SDW in Cr is field independent up to at least 16 T, the spin-flip transition is suppressed with an increasing field in a quadratic and $\boldsymbol{Q}$-direction-dependent manner [32]. The projected critical field for the spin-flip transition at $T = 0$ would be about 25 T, and is expected to be smaller when $T_{SF}$ decreases under pressure. Given that the magnetic field has a tendency to promote the transverse spin configuration [32], it is possible that the spin-flip transition pressure measured under a high field is significantly lower than our zero-field value of $P_c = 1.50 \pm 0.05$ GPa.

Nevertheless, it is unclear how electron and hole ellipsoids in the four-band structure would be affected by a high magnetic field. Although the magnetostriction effect in Cr is negligible for $H < 1$ T, it rises quickly to $\Delta l/l = 1.2 \times 10^{-6}$ under a magnetic field of 2.5 T [44]. By comparison, the relative lattice discontinuities at $T_{SF}(P = 0)$ are only $\Delta l/l = 4$–$5 \times 10^{-6}$ [48], even smaller than the lattice discontinuity at $T_N(P =$

0) ($\Delta l/l = 1\,10^{-5}$) [44]. The lattice change under the high field for dHvA measurements is expected to be no less than lattice discontinuities at the spin-flip transition at $H = 0$.

The complex response of the Fermi surface to the application of large pressures—from changing the electron kinetic energy and thereby affecting the bandwidth of a particular band [27] to inducing charge transfer between bands [28]—is difficult to parse. The combined technique of x-ray magnetic diffraction and Hall measurements provides direct tracking of both the slow charge-transfer process between nesting bands and the overall *P-T* evolution of itinerant charge carriers. Despite the first-order nature of the spin-flip transition, we did not observe significant Fermi surface reconstruction at the quantum phase transition. The approach described here should be generalizable to metals and superconductors where the quantum phase transition may involve non-Fermi liquid behavior or the emergence of exotic ordered states, including even chromium's continuous quantum phase transition between the transverse SDW and the paramagnet at $P \sim 10$ GPa [23].

## ACKNOWLEDGMENTS

We thank R. Jaramillo and J. J. Pluth for their help in sample preparation. The work at the University of Chicago was supported by the National Science Foundation (Grant No. DMR-1206519) and used MRSEC shared facilities (NSF Grant No. DMR-1420709). The work at the Advanced Photon Source of Argonne National Laboratory was supported by the U.S. Department of Energy Basic Energy Sciences under Contract No. NEAC02-06CH11357.

[1] S. Sachdev, *Quantum Phase Transitions*, 2nd ed., Cambridge University Press, Cambridge, UK (2011).
[2] M. Imada, A. Fujimori, and Y. Tokura, Rev. Mod. Phys. **70**, 1039 (1998).
[3] Q. Si, S. Rabello, K. Ingersent, and J. L. Smith, Nature (London) **413**, 804 (2001).
[4] H. V. Löhneysen, A. Rosch, M. Vojta, and P. Wölfle, Rev. Mod. Phys. **79**, 1015 (2007).
[5] E. Rotenberg, B. K. Freelon, H. Koh, A. Bostwick, K. Rossnagel, A. Schmid, and S. D. Kevan, New J. Phys. **7**, 114 (2005).
[6] V. Brouet, W. L. Yang, X. J. Zhou, Z. Hussain, R. G. Moore, R. He, D. H. Lu, Z. X. Shen, J. Laverock, S. B. Dugdale, N. Ru, and I. R. Fisher., Phys. Rev. B **77**, 235104 (2008).
[7] B. L. Altshuler, L. B. Ioffe, and A. J. Millis, Phys. Rev. B **52**, 5563 (1995).
[8] Ar. Abanov and A. V. Chubukov, Phys. Rev. Lett. **84**, 5608 (2000).
[9] M. A. Metlitski and S. Sachdev, Phys. Rev. B **82**, 075128 (2010).
[10] D. Bergeron, D. Chowdhury, M. Punk, S. Sachdev, and A. M. S. Tremblay, Phys. Rev. B. **86**, 155123 (2012).
[11] A. W. Overhauser, Phys. Rev. **128**, 1437 (1962).
[12] T. M. Rice and G. K. Scott, Phys. Rev. Lett. **35**, 120 (1975).
[13] K. McElroy, R. W. Simmonds, J. E. Hoffman, D.-H. Lee, J. Orenstein, H. Eisaki, S. Uchida, and J. C. Davis, Nature (London) **422**, 592 (2003).
[14] A. Janner and T. Janssen, Phys. Rev. B **15**, 643 (1977).
[15] S.-K. Chan and V. Heine, J. Phys. F: Met. Phys. **3**, 795 (1973).
[16] B. C. H. Krutzen and J. E. Inglesfield, J. Phys.: Condens. Matter **2**, 4829 (1990).
[17] M. D. Johannes and I. I. Mazin, Phys. Rev. B **77**, 165135 (2008).
[18] R. J. Elliott and F. A. Wedgwood, Proc. Phys. Soc. **81**, 846 (1963).
[19] G. Ghiringhelli, M. Le Tacon, M. Minola, S. Blanco-Canosa, C. Mazzoli, N. B. Brookes, G. M. De Luca, A. Frano, D. G. Hawthorn, F. He, T. Loew, M. M. Sala, D. C. Peets, M. Salluzzo, E. Schierle, R. Sutarto, G. A. Sawatzky, E. Weschke, B. Keimer, and L. Braicovich, Science **337**, 821 (2012).
[20] J. Chang, E. Blackburn, A. T. Holmes, N. B. Christensen, J. Larsen, J. Mesot, Ruixing Liang, D. A. Bonn, W. N. Hardy, A. Watenphul, M. v. Zimmermann, E. M. Forgan, and S. M. Hayden, Nat. Phys. **8**, 871 (2012).
[21] Y. Feng, J. Wang, D. M. Silevitch, B. Mihaila, J. W. Kim, J.-Q. Yan, R. K. Schulze, N. Woo, A. Palmer, Y. Rena, J. van Wezel, P. B. Littlewood, and T. F. Rosenbaum, Proc. Natl. Acad. Sci. USA **110**, 3287 (2013).
[22] P. B. Littlewood and T. M. Rice, Phys. Rev. Lett. **48**, 44 (1982).
[23] R. Jaramillo, Y. Feng, J. Wang, and T. F. Rosenbaum, Proc. Nat. Acad. Sci. USA **107**, 13631 (2010).
[24] Y. Feng, J. Wang, R. Jaramillo, J. van Wezel, S. Haravifard, G. Srajer, Y. Liu, Z.-A. Xu, P. B. Littlewood, and T. F. Rosenbaum, Proc. Natl. Acad. Sci. USA **109**, 7224 (2012).
[25] L. F. Mattheiss, Phys. Rev. **139**, A1893 (1965).
[26] D. G. Laurent, J. Callaway, J. L. Fry, and N. E. Brener, Phys. Rev. B **23**, 4977 (1981).
[27] Y. Feng, R. Jaramillo, G. Srajer, J. C. Lang, Z. Islam, M. S. Somayazulu, O. G. Shpyrko, J. J. Pluth, H.-k. Mao, E. D. Isaacs, G. Aeppli, and T. F. Rosenbaum, Phys. Rev. Lett. **99**, 137201 (2007).
[28] Y. Feng, J. Wang, A. Palmer, J. A. Aguiar, B. Mihaila, J.-Q. Yan, P. B. Littlewood, and T. F. Rosenbaum, Nat. Commun. **5**, 4218 (2014).
[29] D. Gignoux and D. Schmitt, J. Alloys Compd. **225**, 423 (1995).
[30] T. Hänke, S. Krause, L. Berbil-Bautista, M. Bode, R. Wiesendanger, V. Wagner, D. Lott, and A. Schreyer, Phys. Rev. B **71**, 184407 (2005).
[31] M. Kenzelmann, A. B. Harris, S. Jonas, C. Broholm, J. Schefer, S. B. Kim, C. L. Zhang, S.-W. Cheong, O. P. Vajk, and J. W. Lynn, Phys. Rev. Lett. **95**, 087206 (2005).
[32] Z. Barak, E. Fawcett, D. Feder, G. Lorincz, and M. B. Walker, J. Phys. F: Metal Phys. **11**, 915 (1981).
[33] H. Umebayashi, G. Shirane, B. C. Frazer, and W. B. Daniels, J. Phys. Soc. Jap. **24**, 368 (1968).
[34] Y. Feng, R. Jaramillo, J. Wang, Y. Ren, and T. F. Rosenbaum, Rev. Sci. Instrum. **81**, 041301 (2010).
[35] E. Fawcett, Rev. Mod. Phys. **60**, 209 (1988).
[36] Y. Feng, M. S. Somayazulu, R. Jaramillo, T. F. Rosenbaum, E. D. Isaacs, J. Hu, and H.-k. Mao, Rev. Sci. Instrum. **76**, 063913 (2005).

[37] M. Blume and D. Gibbs, Phys. Rev. B **37**, 1779 (1988).
[38] Y. Furuya, J. Phys. Soc. Jpn. **40**, 490 (1976).
[39] R. Jaramillo, Y. Feng, and T. F. Rosenbaum, Rev. Sci. Instrum. **83**, 103902 (2012).
[40] Y. Feng, D. M. Silevitch, and T. F. Rosenbaum, Rev. Sci. Instrum. **85**, 033901 (2014).
[41] R. D. Barnard, J. Phys. F: Met. Phys. **7**, 673 (1977).
[42] J. Strempfer, Th. Brückel, W. Caliebe, A. Vernes, H. Ebert, W. Prandl, and J. R. Schneider, Eur. Phys. J. B **14**, 63 (2000).
[43] R. L. Stillwell, D. E. Graf, W. A. Coniglio, T. P. Murphy, E. C. Palm, J. H. Park, D. VanGennep, P. Schlottmann, and S. W. Tozer, Phys. Rev. B **88**, 125119 (2013).
[44] E. W. Lee and M. A. Asgar, Phys. Rev. Lett. **22**, 1436 (1969).
[45] W. R. Cox, D. J. Hayes, and F. R. Brotzen, Phys. Rev. B **7**, 3580 (1973).
[46] N. V. Volkenshtein, V. E. Startsev, and V. I. Cherepanov, Phys. Status Solidi B **89**, K53 (1978).
[47] H. Kimura and K. Honda, J. Phys. Soc. Jpn. **31**, 129 (1971).
[48] M. O. Steinitz, L. H. Schwartz, J. A. Marcus, E. Fawcett, and W. A. Reed, Phys. Rev. Lett. **23**, 979 (1969).
[49] Y. Onuki and R. Settai, Low Temp. Phys. **38**, 89 (2012).
[50] P. Walmsley, C. Putzke, L. Malone, I. Guillamón, D. Vignolles, C. Proust, S. Badoux, A. I. Coldea, M. D. Watson, S. Kasahara, Y. Mizukami, T. Shibauchi, Y. Matsuda, and A. Carrington, Phys. Rev. Lett. **110**, 257002 (2013).